IEEE Robotics and Automation Letters (RA-L) paper, presented at ICRA 2026, Vienna, Austria. Cite as RA-L paper.

Nullspace Optimization of Redundant Robots for Dynamics Decoupling in Motion Force Control

Wenbo Tang[1], Shiquan Wang[2], Wenhai Liu[3], and Weiming Wang[1]

***Abstract*—The dynamics coupling between motion and force subspaces in robotic control poses significant challenges to ensuring force control robustness, particularly under large external disturbances. While actively shaping the system inertia can eliminate this coupling, it introduces additional disturbances due to modeling uncertainties and force sensing errors. Inspired by how humans naturally adjust their elbow postures to facilitate motion force operations, we propose a quadratic programming-based nullspace optimization method that minimizes dynamics coupling for redundant torque-controlled robots. Integrated into an impedance motion force control framework, our approach minimizes an objective function defined by the Frobenius norm of the projection matrix representing inertia coupling in Cartesian space, yielding human-like postures that passively decouple task dynamics. Experimental results demonstrate that the proposed nullspace optimization significantly improves force control stability and tracking performance under conditions of high friction and external disturbances, outperforming conventional motion force control with traditional nullspace tracking approaches.**

***Index Terms*—Nullspace optimization, Redundant robots, Dynamics decoupling, Motion force control, Inertia shaping**

I. Introduction

REDUNDANT torque-controlled robots are designed to interact safely with people and environments while leveraging control redundancies for flexible manipulations. These robots possess superior contact force sensing and precise joint torque actuation capabilities, enabling accurate force tracking in various contact scenarios [1]. Fig. 1 illustrates two typical applications of robot interaction in manufacturing and service industries, i.e., surface polishing and body massaging. Such applications require the robot's tool center point (TCP) to simultaneously maintain contact with the environment using desired contact forces while tracking a specific trajectory. The contact dynamics, including surface stiffness, damping, and friction coefficient, can vary significantly during these tasks. Thus, controlling the motion and force simultaneously and robustly is critical to ensuring polishing quality and a satisfactory massaging experience.

Manuscript received: June, 14, 2025; Revised October, 5, 2025; Accepted December, 7, 2025.

This paper was recommended for publication by Clement Gosselin upon evaluation of the Associate Editor and Reviewers' comments. This work was supported by Flexiv Robotics Technology CO.,LTD and the National Natural Science Foundation of China under Grant 52305030.

[1]Wenbo Tang and Weiming Wang are with School of Mechanical Engineering, Shanghai Jiao Tong University, Shanghai, China wenbo.tang@sjtu.edu.cn; wangweiming@sjtu.edu.cn

[2]Shiquan Wang is with Shanghai Flexiv Robotics Technology CO.,LTD, Shanghai, China shiquan.wang@flexiv.com

[3]Wenhai Liu is with School of Artificial Intelligence, Shanghai Jiao Tong University, Shanghai, China sjtu-wenhai@sjtu.edu.cn

Digital Object Identifier (DOI): see top of this page.

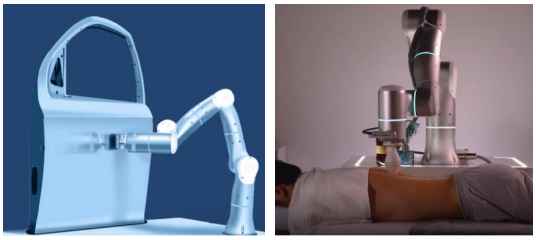

Fig. 1. Two typical applications of redundant robot interaction. On the left, the robot maintains a constant polishing force on the surface while moving along a planned trajectory. On the right, the robot massages a person by applying a dynamic force to a specific body part.

In the context of motion force control, there are two primary categories [2]. The one is the unified approach presented in [3]. It utilizes computed torque control to actuate acceleration in the Cartesian space, but it cannot specify the motion control stiffness and damping. The other one is the wrench projection method proposed in [4], which computes motion and force control wrenches separately and combines them using a projection matrix derived from constrained dynamics. Prioritized control can achieve equivalent outcomes through dynamically consistent nullspace projection [5]. A significant challenge to these approaches is the coupling between motion and force subspaces, which affects the stability and robustness of force control, especially under large disturbances such as friction or unmodeled forces. To address this issue, [6] proposed a hybrid force-impedance control that compensates for the coupled effect within the force subspace. The passivity-based decoupled strategy [7] fully decouples the motion and force subspaces, providing more stability than the unified approach. However, a comparative experimental study [8] showed that an excessive decoupling of the task space reduces control robustness. Another class of approach involves applying impedance control to reshape the robot dynamics, which can be designed to scale the natural inertia [9], completely diagonalize the inertia matrix [10], or comply with constrained task dynamics [11]. However, improper inertia shaping amplifies dynamics uncertainties and magnifies sensor noises [12]. It turns out that every decoupling approach using force feedback can be generalized by inertia shaping through impedance control. The partially decoupled inertia shaping is one of the most effective strategies for achieving the trade-off between maintaining the natural inertia and reducing motion force coupling [13].

Existing solutions for reducing the motion force coupling focus on designing controllers that actively compensate for coupling effects. However, they suffer from the amplification of residual disturbances depending on the amount of shaped dynamics [13]. The ability to reduce the dynamics coupling

IEEE Robotics and Automation Letters (RA-L) paper, presented at ICRA 2026, Vienna, Austria. Cite as RA-L paper.

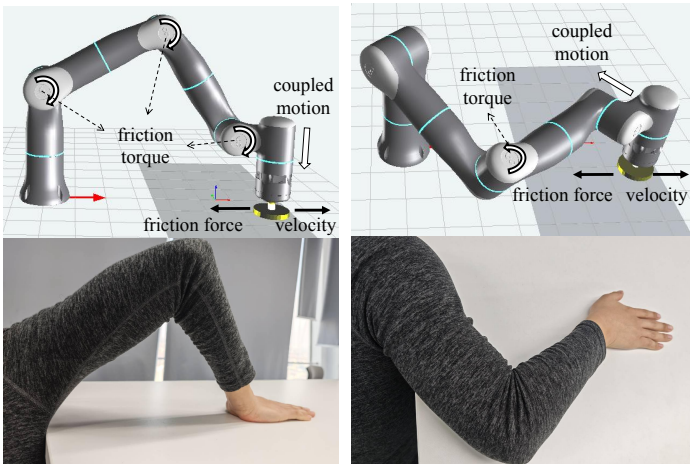

(a) (b)

$$\begin{bmatrix} \Lambda_m & \Lambda_c \\ \Lambda_c^T & \Lambda_f \end{bmatrix} \xrightarrow[\Lambda_c \to 0]{\text{Posture Adaptation}} \begin{bmatrix} \hat{\Lambda}_m & 0 \\ 0 & \hat{\Lambda}_f \end{bmatrix}$$

(c)

Fig. 2. Manipulating the dynamics coupling by changing the posture of redundant arms. (a) The coupled nullspace posture of a redundant robot and its analogous human elbow posture. When the robot attempts to polish forward, the friction resists the motion, causing the joints to rotate. This results in the TCP pushing harder against the surface, increasing the contact force and friction. It is difficult for humans to stably wipe forward on a frictional table in this way. (b) The decoupled nullspace posture of the robot and its analogous human elbow posture. The joint rotation caused by the friction does not make the TCP move along the contact direction. It is easy for humans to wipe forward on the table with a laid-down elbow. (c) Adapting the nullspace posture affects the structure of the task inertia matrix in motion force control.

in non-redundant robots is limited by the unique joint coordinate for a given TCP position. In contrast, redundant robots with more degrees of freedom (DOF) offer an advantage for passively shaping the dynamics by altering the nullspace configuration [14]. This provides the flexibility to improve control performance while interacting with dynamic environments, inspired by the elbow postures of humans during polishing tasks, as shown in Fig. 2. We tend to keep the elbow flat and parallel to the surface while wiping tables, particularly when the friction is high, making it easier to maintain a stable contact and move around. Similarly, appropriate nullspace postures for redundant robots can be identified through nullspace control. The task inertia matrix is divided into blocks in Fig. 2c, including motion subspace Λ_m, force subspace Λ_f, and coupled space Λ_c. The coupling can be reduced or removed through adapting the nullspace posture, obtaining a block-diagonal inertia matrix with changed block $\hat{\Lambda}_m$ and $\hat{\Lambda}_f$.

Nullspace control for redundant torque-controlled robots is mainly based on hierarchical torque projection [15]. Priorities of the tasks can be extended to the dynamics level, deriving the dynamically consistent Jacobian pseudoinverse and torque projection matrix [16]. Hierarchical control based on task priority can combine with compliance control to accomplish whole-body tasks in contact environments [17]. The stability of the multi-level compliance controller for both task space and nullspace of redundant robots has been demonstrated using a semi-definite Lyapunov function [18]. The nullspace can integrate an arbitrary multi-task hierarchical decoupling control framework, including collision avoidance through potential field control [19], nullspace compliance control [20], etc. Quadratic programming (QP) is an appealing approach for nullspace control of redundant robots to incorporate inequality constraints on joint position, velocity, and acceleration [21]. One approach to achieving multi-task Cartesian space impedance control is through prioritized QP, which avoids matrix pseudoinverse calculations while considering various constraints [22]. It is also possible to exploit QP to adapt the constrained stiffness in the impedance-based force controller to track the desired force profiles within a hierarchical impedance control framework [23]. The general inverse solutions of redundant robots obtained by solving a QP problem can incorporate manipulability maximization, joint limit inequality constraints, and obstacle avoidance objectives [24]. Kinematic control based on QP nullspace optimization has also been studied in static/dynamic obstacle avoidance [25]. Although various nullspace control applications have been investigated, a unified framework for both active and passive regulation of system dynamics in motion force control is still lacking.

This work fills this gap by addressing two key challenges. The first is the online adaptation of nullspace posture for dynamics decoupling during motion force control. In a hierarchical control framework, we employ impedance control as the primary task for decoupled inertia shaping. The nullspace goal velocity is generated by minimizing the dynamics coupling-oriented objective function through online QP optimization. The second challenge lies in determining an appropriate objective function representing the dynamics coupling. We propose several representations to evaluate the magnitude of coupling and derive the gradients. The most suitable form is determined through comparative simulations. Experimental results demonstrate that our approach significantly improves force control stability and tracking performance in tasks subject to high frictions and large disturbances.

The remainder of this paper is organized as follows: Section II elaborates on the multi-task hierarchical control framework that integrates the decoupled impedance motion force control and nullspace posture control. The QP-based nullspace optimization problem exploiting the gradients of different motion force coupling objectives is presented in Section III. Comparisons of nullspace postures and force control performances across various nullspace optimization objectives are discussed in Section IV through simulations and experiments. Finally, section V concludes the paper.

II. Motion Force Control of Redundant Robots

A. Control Task Hierarchy and Task Space Dynamics

The rigid-body dynamics of a redundant manipulator with $n > 6$ DOF can be expressed as [6]

$$M(q)\ddot{q} + \mu(q, \dot{q}) = \tau + \tau^e \,, \tag{1}$$

with the generalized joint position coordinates q, the inertia matrix $M(q)$, the Coriolis and gravity torque $\mu(q, \dot{q})$. The quantities τ, τ^e describe the actuation torque and the external

IEEE Robotics and Automation Letters (RA-L) paper, presented at ICRA 2026, Vienna, Austria. Cite as RA-L paper.

torque. Two hierarchical tasks control the joints of the redundant robots. The primary task defines the Cartesian coordinates x via the mapping $x = f_x(q)$. The Jacobian matrix $J(q)$ maps from joint velocities to Cartesian velocities, i.e.,

$$\dot{x} = J(q)\dot{q} \ , \quad J(q) = \partial f_x(q)/\partial q \ . \tag{2}$$

In a common singularity-free workspace, the dynamically consistent generalized inverse of $J(q)$ is $\bar{J}(q) = M^{-1}J^T(JM^{-1}J^T)^{-1}$. Multiplying both sides of (1) by $\bar{J}(q)^T$ obtains the Cartesian task dynamics [16]

$$\Lambda_x \ddot{x} + \mu_x = F_x + F_x^e \ , \tag{3}$$

where Λ_x is the Cartesian task inertia matrix, μ_x is the task Coriolis and gravity forces. The Cartesian task forces consist of the actuation force F_x and the external force F_x^e.

The secondary task controls the joint velocities $\dot{q}_n$ in the dynamically consistent nullspace of the primary task $N(q)$

$$\dot{q}_n = N(q)\dot{q} \ , \quad N(q) = I - \bar{J}(q)J(q) \ , \tag{4}$$

with I being the $n \times n$ identity matrix. The dynamically consistent generalized inverse of $N(q)$ is $\bar{N}(q) = M^{-1}N^T(NM^{-1}N^T)^{\#}$, where $\#$ is the Moore-Penrose pseudoinverse of a matrix. Instead of introducing a reduced set of controllable coordinates from $N(q)$ for nullspace impedance control [5], a more straightforward secondary task dynamics for acceleration control can be obtained through multiplying both sides of (1) by $\bar{N}(q)^T$ [16]

$$\Lambda_n \ddot{q}_n + \mu_n = F_n + F_n^e \ , \tag{5}$$

where $\Lambda_n = (NM^{-1}N^T)^{\#}$ is the nullspace task inertia matrix that can project the task acceleration to the controllable directions of the nullspace task, μ_n is the task Coriolis and gravity forces. The nullspace task forces consist of the actuation force F_n and the external force F_n^e.

B. Decoupled Motion Force and Nullspace Control

The inertia Λ_x can be divided into motion subspace A, coupled subspace B, and force subspace D [13]. x and F_x^e can be separated into the motion subspace with subscript m and the force subspace with subscript f

$$\Lambda_x = \begin{bmatrix} A & B \\ B^T & D \end{bmatrix} \ , \quad x = \begin{bmatrix} x_m \\ x_f \end{bmatrix} \ , \quad F_x^e = \begin{bmatrix} F_m^e \\ F_f^e \end{bmatrix} \ . \tag{6}$$

Assuming that μ_x is canceled by F_x, a non-zero contact wrench in the motion subspace generates coupled acceleration in the force subspace if B^T exists. To eliminate this coupling, the ideal impedance control law $\hat{F}_x$ is [9]

$$\hat{F}_x = \Lambda_x \hat{\Lambda}_x^{-1} u + (\Lambda_x \hat{\Lambda}_x^{-1} - I)F_x^e + \mu_x \ , \tag{7}$$

where $\hat{\Lambda}_x$ is the desired inertia that removes the coupling. However, disturbances ϵ from model uncertainties and sensing noises exist in the controller, making $F_x = \hat{F}_x - \epsilon$. The shaped task dynamics with the new control input u becomes

$$\hat{\Lambda}_x \ddot{x} = u + F_x^e - \epsilon + (I - \hat{\Lambda}_x \Lambda_x^{-1})\epsilon \ , \tag{8}$$

showing that inertia shaping amplifies ϵ through the projection matrix $I - \hat{\Lambda}_x \Lambda_x^{-1}$, which vanishes only if $\hat{\Lambda}_x = \Lambda_x$. Thus, the desired inertia should be as close to the natural inertia as possible [12]. This paper chooses the asymmetric partially decoupled form that has the least disturbance amplification while achieving motion force decoupling [13].

$$\hat{\Lambda}_x = \begin{bmatrix} A & B \\ 0 & \hat{D} \end{bmatrix} \ , \quad \hat{D} = D - B^T A^{-1} B \ , \tag{9}$$

and the disturbance projection matrix becomes

$$I - \hat{\Lambda}_x \Lambda_x^{-1} = \begin{bmatrix} 0 & 0 \\ B^T A^{-1} & 0 \end{bmatrix} \ . \tag{10}$$

The inertia form (9) exactly removes the force coupling, but keeps the motion dynamics unchanged, which is internally equivalent to prioritized force and motion control [13]. The asymptotic stability can be proved through the conditional stability analysis [18]. The new control input $u = [u_m^T \ u_f^T]^T$ consists of the motion subspace u_m and the force subspace u_f. The motion subspace uses Cartesian impedance motion control [5] to track the desired trajectory $\hat{x}_m$

$$u_m = A\ddot{\hat{x}}_m + (K_m^d + C_m)\dot{e}_m + K_m^p e_m \ , \tag{11}$$

where $e_m = \hat{x}_m - x_m$. K_m^p and K_m^d are the positive definite proportional and damping gain matrices to preserve a constant damping ratio ζ. C_m can be any arbitrary matrix, for which the skew symmetry of $\dot{A} - 2C_m$ holds.

The force subspace uses explicit force control [13] with task velocity damping to track the desired contact force $\hat{F}_f^e$

$$u_f = -\hat{F}_f^e + K_f^p e_f - (K_f^d + C_f)\dot{x}_f + K_f^i \int e_f \ , \tag{12}$$

where $e_f = F_f^e - \hat{F}_f^e$. K_f^p, K_f^d, and K_f^i are respectively positive definite force proportional gain, velocity damping, and force integral gain matrices, C_f can be any arbitrary matrix, for which the skew symmetry of $\dot{\hat{D}} - 2C_f$ holds.

The nullspace posture task uses computed torque control [17] to track the goal nullspace velocity $\hat{\dot{q}}_n$

$$F_n = \Lambda_n K_n^d (\hat{\dot{q}}_n - \dot{q}_n) + \mu_n \ , \tag{13}$$

with K_q^d being a positive definite velocity control gain. The total torque τ is the sum of the projected control torques

$$\tau = J^T F_x + N^T F_n \ . \tag{14}$$

III. Nullspace Optimization Control Design

A. Nullspace Velocity Optimization Problem

Solving the goal nullspace velocity $\hat{\dot{q}}_n$ can be formulated into a QP with the objective function $f(\hat{\dot{q}}_n)$ [25]

$$\min_{\hat{\dot{q}}_n} \ f(\hat{\dot{q}}_n) = \frac{1}{2}\hat{\dot{q}}_n^T Q \hat{\dot{q}}_n + k_0 \left(\frac{\partial W(q)}{\partial q}\right)^T \hat{\dot{q}}_n \ . \tag{15}$$

The objective matrix $Q = I$ means that every joint velocity norm is weighted the same during the optimization. The preferred joint velocities can be obtained by scaling the gradient of an additional minimization objective $W(q)$ by a positive factor k_0, which determines the convergence speed to the local minimum of $W(q)$. Considering the task hierarchy, the joint velocities should be optimized in the dynamically

IEEE Robotics and Automation Letters (RA-L) paper, presented at ICRA 2026, Vienna, Austria. Cite as RA-L paper.

consistent nullspace of the primary task, ensuring that the result is feasible for nullspace control. Therefore, the following equality constraint should be satisfied

$$J(q)\hat{\dot{q}}_n = 0 \ . \tag{16}$$

Besides, the joint velocities should be within the maximum physical limits, bringing the inequality constraints

$$\dot{q}_{min} < \hat{\dot{q}}_n < \dot{q}_{max} \ , \tag{17}$$

where $\dot{q}_{min}$ and $\dot{q}_{max}$ are the vectors representing the minimum and maximum joint velocity for each joint. (15), (16) and (17) constitute the entire QP problem to generate the desired velocity for the nullspace posture task.

B. Optimization Objectives for Motion Force Decoupling

The common nullspace compliance control [22][23] with desired joint position q_d can be integrated into the QP by minimizing the joint position distance $W(q)_j$

$$W(q)_j = \frac{(q-q_d)^T(q-q_d)}{2} \ , \quad \frac{\partial W(q)_j}{\partial q} = q - q_d \ . \tag{18}$$

In this paper, $W(q)$ can be exploited to minimize the motion force coupling, which initially comes from the off-diagonal terms of the task space inertia matrix. Changing the nullspace posture passively shapes the inertia matrix while keeping the acceleration of the Cartesian task unaffected. However, the coupling projection to be considered is not unique, depending on the selected spaces of the projection.

Given Λ_x in (6), defining selection matrices

$$S_m = \begin{bmatrix} I & 0 \end{bmatrix} \ , \quad S_f = \begin{bmatrix} 0 & I \end{bmatrix} \ , \tag{19}$$

the inertia matrix block A and B^T can be represented as

$$A = S_m \Lambda_x S_m^T \ , \quad B^T = S_f \Lambda_x S_m^T \ . \tag{20}$$

Table I lists three types of projection matrices P_f, P_a, and P_d, considered to represent motion force coupling. The first option is to optimize the coupling term $P_f = S_f \Lambda_x^{-1} S_m^T$, which decides the amount of coupled accelerations to the force subspace from an unintended contact wrench with unit norm in the motion subspace. Decreasing B or increasing A and $\hat{D}$ can reduce this type of coupling. A more straightforward choice is to optimize the coupled inertia $P_a = B^T$, which represents the wrench in the force subspace required to generate an acceleration of unit norm in the motion subspace. The advantage of using P_a is that B^T alone directly reflects the off-diagonal dynamics coupling in the inertia matrix. Alternatively, considering the disturbance amplification from inertia shaping in the impedance motion force control, the coupling term $P_d = B^T A^{-1}$ in (10) could be optimized to minimize the disturbance sensitivity of inertia shaping, i.e., the additional disturbance introduced in the shaped task dynamics from a raw disturbance wrench with unit norm. Besides lowering B, making the motion subspace inertia A larger can also reduce the disturbance amplification.

Given a coupling projection matrix, the optimization objective $W(q)$ should be defined to evaluate the coupling magnitude. For an arbitrary space projection $y = Pv$, the set of vectors v and y satisfying

$$v^T v = y^T (PP^T)^{-1} y = 1 \ , \tag{21}$$

describes the points on the unit sphere surface in v space and the points on the projected ellipsoid surface in y space. The lengths of the ellipsoid's principal axes are determined by the eigenvalues σ_i, for $i = 1, \cdots, r$, of the matrix PP^T, where r is its dimension. Fig. 3 visualizes the projection in the two-dimensional space. Minimizing the coupling projection means that the ellipsoid should be shrunk toward a point as much as possible, which brings the minimization objective

$$W(q) = \sum_{i=1}^{r} \sigma_i = ||P||_F^2 \ , \tag{22}$$

with $||P||_F$ being the Frobenius norm of P. Therefore, the objectives corresponding to the three coupling projections are $W(q)_f = ||P_f||_F^2$, $W(q)_a = ||P_a||_F^2$, and $W(q)_d = ||P_d||_F^2$.

TABLE I
PROJECTION MATRICES IN MOTION FORCE COUPLING

Matrix	Representation	Physical Intuition
P_f	$S_f \Lambda_x^{-1} S_m^T$	TCP acceleration in the force subspace generated by contact wrench in the motion subspace
P_a	$S_f \Lambda_x S_m^T$	Actuation wrench in the force subspace to generate acceleration in the motion subspace
P_d	$S_f \Lambda_x S_m^T (S_m \Lambda_x S_m^T)^{-1}$	Additional disturbance wrench introduced by inertia shaping

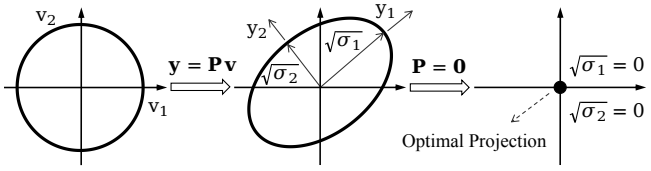

Fig. 3. Matrix projection in the two-dimensional space. The projection matrix $P = 0$ minimizes the magnitude of the motion force coupling, causing the projected ellipsoid to collapse into a point at the origin.

C. Gradients of Optimization Objectives

Once the additional optimization objective has been defined, the objective vector in (15) can be obtained from the gradient of $W(q)$ to the joint positions q

$$\frac{\partial W(q)}{\partial q} = \begin{bmatrix} \frac{\partial W(q)}{\partial q_1} & \cdots & \frac{\partial W(q)}{\partial q_n} \end{bmatrix}^T \ , \tag{23}$$

where the gradient to the kth joint position q_k is

$$\frac{\partial W(q)}{\partial q_k} = \sum_i \sum_j \left(2P \circ \frac{\partial P}{\partial q_k} \right)_{ij} \ , \tag{24}$$

IEEE Robotics and Automation Letters (RA-L) paper, presented at ICRA 2026, Vienna, Austria. Cite as RA-L paper.

TABLE II
MOTION FORCE CONTROL PARAMETERS

Parameters	Simulation	Experiment
Force K_f^p	0.5	0.25
Force K_f^d	200	300
Force K_f^i	0	10
Desired $\hat{F}_f^e$	20N	
Motion K_m^p	[4000, 4000, 4000 N/m, 400, 400, 400 Nm/rad]	
Motion ζ	[0.7, 0.7, 0.7, 0.7, 0.7, 0.7]	
Motion K_q^p	[50, 50, 50, 50, 50, 50, 50]	

with the element-wise product of two matrices $\circ$, and $\sum_i \sum_j$ represents the sum of all matrix elements. For the projection matrices listed in Table I, the gradients to q_k are

$$\frac{\partial P_f}{\partial q_k} = -S_f \Lambda_x^{-1} \frac{\partial \Lambda_x}{\partial q_k} \Lambda_x^{-1} S_m^T \,, \tag{25}$$

$$\frac{\partial P_a}{\partial q_k} = S_f \frac{\partial \Lambda_x}{\partial q_k} S_m^T \,, \tag{26}$$

$$\frac{\partial P_d}{\partial q_k} = \left(S_f - B^T A^{-1} S_m\right) \frac{\partial \Lambda_x}{\partial q_k} S_m^T A^{-1} \,. \tag{27}$$

where the gradients $\partial \Lambda_x / \partial q_k$ can be computed numerically. Introducing these gradients into (24) gives the objective vectors for the QP optimization.

IV. SIMULATIONS AND EXPERIMENTS

The nullspace optimization for motion force decoupling was studied through both simulations and experiments using the torque-controlled Flexiv Rizon4s robot with 7-DOF. The simulations used an accurate robot dynamics model that was injected with various sensing disturbances. The experiments were conducted with the robot polishing a surface using either an electric or a passive polishing tool. The Cartesian spaces are arranged as [PX, PY, PZ, RX, RY, RZ], where the first and last three spaces are translation and rotation subspaces along the X, Y, and Z axes. The PZ axis belongs to the force subspace, leaving the other axes in the motion subspace. Table II lists the details of the control design.

A. Simulation and Experimental Setups

Fig. 4 shows the self-developed simulation platform of the Rizon4s robot and a virtual surface supporting point contact. The robot dynamics including motor inertia were accurately modeled in the controller. The contact stiffness of the surface was 30000 N/m while no contact damping existed. Coulomb friction was simulated to introduce a coupling force from the motion subspace. Two Coulomb friction coefficients $\mu = 0.25$ and 1.0 were simulated to evaluate the control performances under different motion force coupling magnitudes. The simulated contact force was disturbed by a zero-mean Gaussian random noise with 5N variance and a 1Hz sinusoidal disturbance with 2N amplitude. The simulated sensor was filtered by a 1st-order low-pass filter with 25Hz cutoff frequency.

To investigate the advantages of nullspace optimization under sensing noise and large external disturbances, the robot

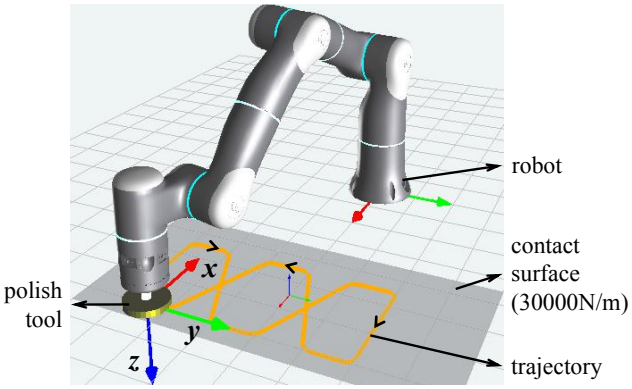

Fig. 4. Simulation platform. The robot moved along a horizontal trajectory on the XY plane while controlling the contact force against the surface. The contact was simulated using a single point at the TCP and a spring model of the flat surface with a stiffness of 30000N/m. The Coulomb friction was generated online based on the spring force and the direction of TCP velocity.

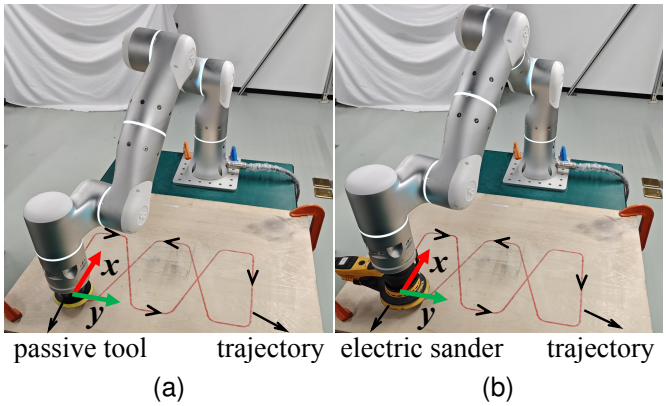

Fig. 5. Experiment platform with a flat wooden surface. (a) A passive tool was installed on the flange. (b) An electric sander was installed on the flange. Both model uncertainties and force-sensing disturbances existed. The passive tool generated friction forces between the sandpapers and the wooden board. The electric sander introduced high-frequency external disturbances due to eccentricity but negligible friction.

with a force sensor at the flange performing polishing tasks along a given trajectory on a flat contact surface was tested. The force sensor was calibrated using the gravity of the passive tool as a baseline when the TCP was static. The tool gravity was calculated and compensated online in the force measurements based on TCP orientations. The cutoff frequency of the 1st-order low pass filter on the force sensing is 25Hz. As shown in Fig. 5a, the passive polishing tool installed two sandpapers having different friction coefficients $\mu = 0.25$ and 0.75 to verify the influence of motion force coupling magnitude on the force control stability. Besides, the control performances under large external disturbances were assessed by mounting a Mirka DEOS electric sander at the flange with 7000 RPM, as presented in Fig. 5b.

B. Simulations and Discussion

During the simulation, the robot first established contact with the surface using the same initial posture as shown in Fig. 6a. Then, it optimized its posture using various optimization

IEEE Robotics and Automation Letters (RA-L) paper, presented at ICRA 2026, Vienna, Austria. Cite as RA-L paper.

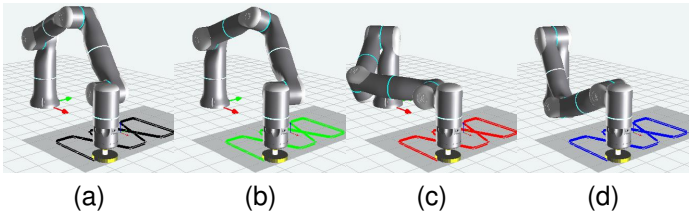

Fig. 6. Optimized postures of the simulation at the trajectory start. (a) The desired posture for the objective $W(q)_j$. (b) Optimized posture using the coupling objective of the inertia matrix inverse $W(q)_f$. (c) Optimized posture using the coupling objective of the inertia matrix $W(q)_a$. (d) Optimized posture using the disturbance coupling objective $W(q)_d$.

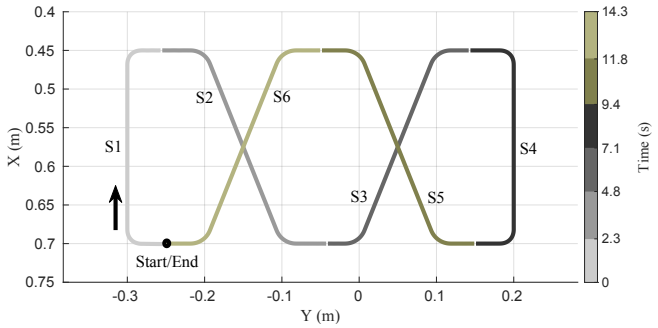

Fig. 7. The XY position command of the trajectory. The trajectory was divided into six segments (S1 to S6) based on the movement direction along the X-axis. The duration of each segment is indicated in the color bar.

objectives while keeping the TCP static until the robot configuration converged to the final postures shown in Fig. 6. Since the objective $W(q)_j$ used the same initial posture as the joint position command, the robot converged instantly with its posture unchanged. Optimizing $W(q)_f$ slightly pushed the robot's elbow to the right, while the gradient of $W(q)_a$ actuated the robot to lower its elbow to the left by approximately 90 degrees, resulting in a final configuration similar to the human arm when polishing the horizontal surface. The objective that induced the most significant change in nullspace posture is $W(q)_d$, which inverted the elbow from top to bottom.

After the robot configuration converged from the initial posture, the TCP started to move along the trajectory in Fig. 7 while optimizing the nullspace posture online. As shown in Fig. 8, all three motion force coupling magnitudes were computed and plotted in three rows, when using different nullspace optimization objectives represented by different colors. The changing patterns of all coupling magnitudes align with the trajectory segments. When the QP adopted $W(q)_j$ as the optimization objective, none of the coupling magnitudes shown in black reached their minimum mean or max values, as the robot merely maintained the nullspace posture at its initial value. When $W(q)_f$ was injected into the QP, both the mean and max of its magnitude shown in green were the minimum during the polishing task. But the other two coupling magnitudes remained as high as the case with $W(q)_j$ optimized. When $W(q)_a$ was optimized, its mean and max were substantially reduced to below 3, as indicated by the red line. This demonstrates that the posture in 6c with a flat elbow can decouple the motion force task space inertia

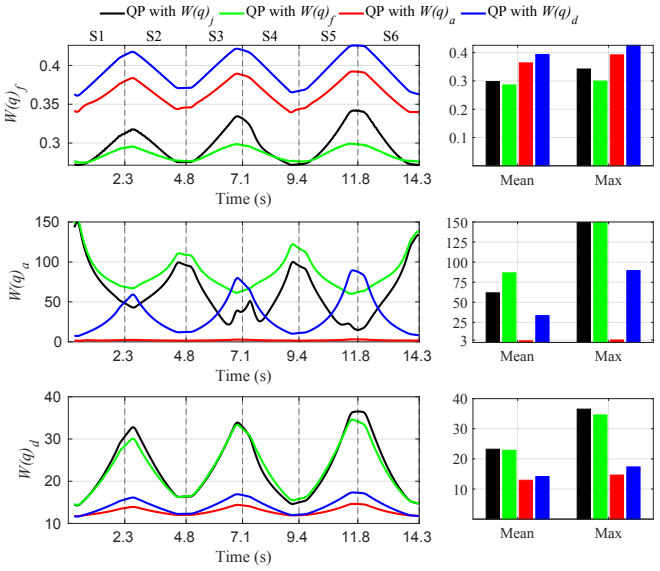

Fig. 8. Online changing values of all three motion force coupling objectives during the simulations. The plots simultaneously record the coupling objectives $W(q)_f$, $W(q)_a$, and $W(q)_d$, when the QP adopted the four optimization objectives distinguished by different colors. The mean and max objective values are compared through the bar charts.

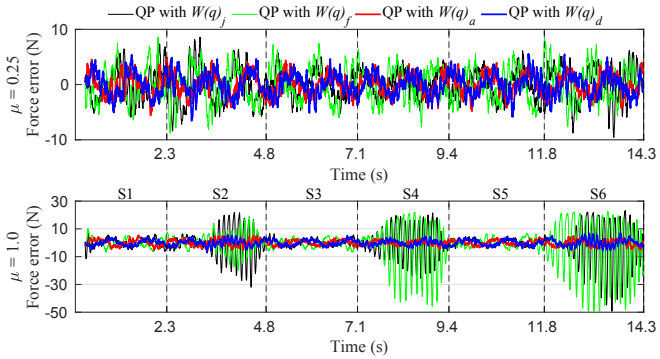

Fig. 9. Force tracking errors of the simulations with two Coulomb friction coefficients μ. The force error is the difference between the desired force of 20N and the filtered contact force. The top plot shows the force error when $\mu = 0.25$, and the bottom plot records the data when $\mu = 1$.

better than other postures. Meanwhile, even the magnitude of the disturbance coupling in motion force control $W(q)_d$ across the polishing task was lower than the case that took the magnitude itself as the optimization objective shown in blue. The discrepancy arose because posture optimization tends to converge to the local minimum rather than a global one. Although the initial values of $W(q)_d$ were the same for the QP with objectives $W(q)_a$ and $W(q)_d$, optimizations starting from different postures shown in Fig. 6 converged to different nullspace configurations and coupling magnitude values. For a fixed TCP pose, the nullspace of the 7-DOF robot is topologically equivalent to a line. This allows the global minimum to be found by searching along the nullspace. For a given TCP trajectory, a globally optimal nullspace path can be planned offline on the continuous nullspace surface by optimizing an objective function over the entire trajectory.

IEEE Robotics and Automation Letters (RA-L) paper, presented at ICRA 2026, Vienna, Austria. Cite as RA-L paper.

TABLE III
STATISTICAL FORCE ERROR (N) OF THE SIMULATION

Cases	$\mu = 0.25$			$\mu = 1.0$		
$W(q)$	MA	PTP	STD	MA	PTP	STD
$W(q)_j$	2.3	18.2	2.8	5.9	72.4	9.3
$W(q)_f$	2.5	17.4	3.1	7.4	74.0	12.0
$\boxed{W(q)_a}$	1.5	10.5	1.8	1.6	10.8	2.0
$W(q)_d$	1.6	12.2	2.0	1.8	14.1	2.1

TABLE IV
SELECTION OF OBJECTIVE FOR MOTION FORCE DECOUPLING

Optimization Objectives	Force Control Performance	Human-like Posture	Motion Force Decoupling
$W(q)_j$	×	×	×
$W(q)_f$	×	×	✓
$\boxed{W(q)_a}$	✓	✓	✓
$W(q)_d$	✓	×	×

For the robot performing the polishing task, the larger the Coulomb friction coefficient μ, the stronger the motion force coupling effect. As shown in Fig. 9, all simulations using QP with the four optimization objectives achieved stable and acceptable force tracking performance when $\mu = 0.25$. However, when the nullspace posture was optimized based on $W(q)_j$ shown in black or $W(q)_f$ shown in green, the system became oscillatory and unstable when $\mu = 1$ and four times larger coupling were generated with the same contact force. Notably, the oscillations only occurred during trajectory segments S2, S4, and S6, when the robot was stretching forward along the X-axis. In these segments, positive feedback existed between the friction and the coupled contact force, meaning that larger friction caused the TCP to push harder against the surface. The system could easily become unstable if disturbances, especially time delays, exist in the force sensing for inertia shaping. During trajectory segments S1, S3, and S5, the friction tended to lift the TCP and reduce the contact force, enhancing the force control stability under sensing disturbances. On the other hand, the optimization using $W(q)_a$ shown in red, or $W(q)_d$ shown in blue, maintained stable force control and consistent tracking performance. Table III presents the statistical force tracking results of the simulation. Although optimizing $W(q)_f$ obtained the minimum objective value as shown in Fig. 8, the force tracking became worse compared to the case optimizing $W(q)_j$, as indicated by the larger mean absolute (MA) value, peak-to-peak (PTP) value, and standard deviation (STD) of the force error when $\mu = 1.0$. It suggests that minimizing $W(q)_f$ is not appropriate for motion force decoupling. On the contrary, the force tracking performance under optimized $W(q)_a$ or $W(q)_d$ was superior to the previous two cases and nearly unaffected by the Coulomb friction. The improvement stems from the reduction of motion force coupling, making the force control less sensitive to coupled disturbances. Given the differences between the optimization objectives from various perspectives, we selected the most appropriate one for the experiments. As shown in Table IV, $W(q)_a$ was chosen as the final representation of the optimization objective due to its best force tracking, most human-like posture, and lower motion force coupling magnitudes than $W(q)_d$.

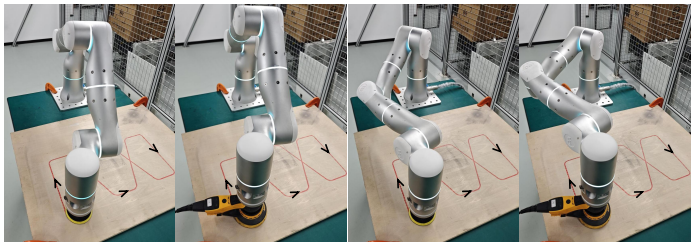

Fig. 10. Optimized postures of the flat surface experiments at the trajectory start using different optimization objectives. (a) The initial and desired postures for $W(q)_j$. (b) Optimized postures using the objective $W(q)_a$.

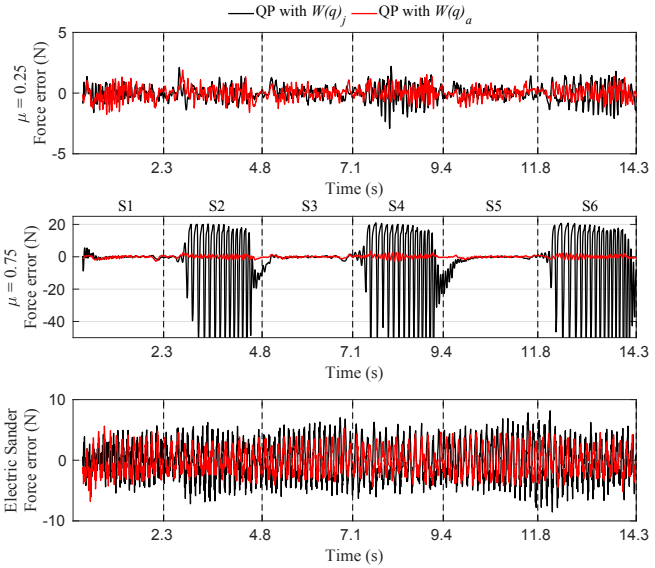

Fig. 11. Force tracking errors of the experiments on the flat surface. The upper two plots show the errors when using the passive polishing tool with two different sandpapers, having friction coefficients of $\mu = 0.25$ and 0.75. The bottom plot shows the force error when the electric sander was installed.

C. Experiments and Discussion

Since the experiments on the flat surface used the same TCP trajectory as the simulation, the objective values of motion force coupling in Fig. 8 were identical for both cases. The initial robot postures when the TCP reached the trajectory start and the optimized postures using nullspace optimization objective $W(q)_a$ are presented in Fig. 10, which are nearly the same as the postures in Fig. 6. It turned out that if the nullspace attempted to maintain its initial joint configuration through optimizing $W(q)_j$, the unstable force-tracking behavior observed after increasing the contact friction coefficient could be well reproduced in the experiment, as shown in Fig. 11. When the sandpaper with a lower $\mu = 0.25$ was installed on the passive polishing tool, both force tracking using optimization objectives $W(q)_j$ shown in black and $W(q)_a$ shown in red were stable. The force statistical errors of nullspace optimization

IEEE Robotics and Automation Letters (RA-L) paper, presented at ICRA 2026, Vienna, Austria. Cite as RA-L paper.

TABLE V
STATISTICAL FORCE ERROR (N) OF THE EXPERIMENTS

Cases	$\mu = 0.25$		$\mu = 0.75$		Electric Sander	
$W(q)$	$W(q)_j$	$\boxed{W(q)_a}$	$W(q)_j$	$\boxed{W(q)_a}$	$W(q)_j$	$\boxed{W(q)_a}$
MA	0.5	0.4	10.0	0.6	2.6	1.8
PTP	5.1	3.7	97.0	6.1	16.7	12.4
STD	0.6	0.5	17.0	0.8	3.1	2.1

using $W(q)_a$ given in Table V have negligible improvement compared to that of $W(q)_j$. However, the comparison in the case of $\mu = 0.75$ indicated that optimizing the objective $W(q)_a$ in the nullspace can significantly improve the stability of the force control system. The force error only increased by half after the friction increased, whereas the $W(q)_j$ optimized nullspace control resulted in TCP jumping and oscillation during the polishing. From the result when using the electric sander with negligible friction in Fig. 11, the amplitude of the force error vibration caused by disturbances from the rotating sander was lower through optimizing $W(q)_a$. The reduced force statistical errors in Table V demonstrate the superiority of motion force coupling minimization in rejecting external disturbances during the motion force control.

While validated on the presented polishing task, the proposed approach is general and can be directly applied to other contact-rich tasks (e.g., wiping or assembly) that similarly require stable force interaction. Furthermore, the nullspace optimization for motion force decoupling is scalable to higher-DOF robots, as the proposed objective function remains valid. The increased redundancy in such robots provides a larger nullspace, potentially enabling even better dynamic decoupling. The method is also applicable to non-planar environments, since the formulation is defined in the task space and can be adapted to surface geometries.

V. CONCLUSIONS

The proposed nullspace optimization framework provides a systematic and effective approach to improving decoupled motion force control in redundant torque-controlled robots. Based on a QP-based nullspace control strategy, the method minimizes dynamics coupling by posture adaptation according to a coupling-oriented objective function, thereby enhancing force tracking stability and reducing sensitivity to external disturbances and friction. The decoupling framework achieves superior performance in maintaining force control stability compared to conventional nullspace control strategies, which are often prone to contact force oscillations. The optimization process consistently identifies nullspace postures with lower coupling magnitudes, frequently resembling human elbow configurations during surface polishing tasks. This observation offers a biomechanical perspective on efficient force control, which suggests the applicability to robots with higher degrees of redundancy, including mobile manipulators and humanoid systems. Such platforms could benefit from the ability to dynamically adapt nullspace to complex contact conditions, thereby enhancing force control precision and robustness.

REFERENCES

[1] S. Haddadin and E. Shahriari, "Unified force-impedance control," *IJRR*, vol. 43, no. 13, pp. 2112–2141, 2024.

[2] V. Ortenzi, R. Stolkin, J. Kuo, and M. Mistry, "Hybrid motion/force control: a review," *Advanced Robotics*, vol. 31, pp. 1102–1113, 2017.

[3] O. Khatib, "A unified approach for motion and force control of robot manipulators: The operational space formulation," *IEEE Journal on Robotics and Automation*, vol. 3, no. 1, pp. 43–53, 1987.

[4] V. Ortenzi, M. Adjigble, J. A. Kuo, R. Stolkin, and M. Mistry, "An experimental study of robot control during environmental contacts based on projected operational space dynamics," in *2014 Humanoids*. IEEE, pp. 407–412.

[5] A. Dietrich and C. Ott, "Hierarchical impedance-based tracking control of kinematically redundant robots," *IEEE TRO*, vol. 36, no. 1, pp. 204–221, 2019.

[6] M. Iskandar, C. Ott, A. Albu-Schäffer, B. Siciliano, and A. Dietrich, "Hybrid force-impedance control for fast end-effector motions," *IEEE RA-L*, vol. 8, no. 7, pp. 3931–3938, 2023.

[7] X. Wu, C. Ott, A. Albu-Schäffer, and A. Dietrich, "Passive decoupled multitask controller for redundant robots," *IEEE Transactions on Control Systems Technology*, vol. 31, no. 1, pp. 1–16, 2022.

[8] X. Wu, C. Ott, and A. Dietrich, "A comparative experimental study of multi-tasking tracking and interaction control on a torque-controlled humanoid robot," in *2022 ACC*. IEEE, pp. 1933–1940.

[9] S. Fahmi and T. Hulin, "Inertial properties in haptic devices: Non-linear inertia shaping vs. force feedforward," *IFAC*, vol. 51, 2018.

[10] Y. Lin, Z. Chen, and B. Yao, "Unified method for task-space motion/force/impedance control of manipulator with unknown contact reaction strategy," *IEEE RA-L*, vol. 7, no. 2, pp. 1478–1485, 2021.

[11] J. Lachner, F. Allmendinger, S. Stramigioli, and N. Hogan, "Shaping impedances to comply with constrained task dynamics," *IEEE TRO*, vol. 38, no. 5, pp. 2750–2767, 2022.

[12] A. Dietrich, X. Wu, K. Bussmann, M. Harder, M. Iskandar, J. Englsberger, C. Ott, and A. Albu-Schäffer, "Practical consequences of inertia shaping for interaction and tracking in robot control," *Control Engineering Practice*, vol. 114, p. 104875, 2021.

[13] W. Tang, W. Wang, and S. Wang, "Partially decoupled impedance motion force control using prioritized inertia shaping," *IEEE RA-L*, vol. 9, no. 9, pp. 7621–7628, 2024.

[14] H. Khurana and A. Billard, "Motion planning and inertia-based control for impact aware manipulation," *IEEE TRO*, vol. 40, 2024.

[15] A. Dietrich, C. Ott, and A. Albu-Schäffer, "An overview of null space projections for redundant, torque-controlled robots," *IJRR*, vol. 34, no. 11, pp. 1385–1400, 2015.

[16] O. Khatib, L. Sentis, J. Park, and J. Warren, "Whole-body dynamic behavior and control of human-like robots," *International Journal of Humanoid Robotics*, vol. 1, no. 01, pp. 29–43, 2004.

[17] L. Sentis and O. Khatib, "Synthesis of whole-body behaviors through hierarchical control of behavioral primitives," *International Journal of Humanoid Robotics*, vol. 2, no. 04, pp. 505–518, 2005.

[18] C. Ott, A. Dietrich, and A. Albu-Schaffer, "Prioritized multi-task compliance control of redundant manipulators," *Automatica*, vol. 53, pp. 416–423, 2015.

[19] A. Dietrich, T. Wimbock, A. Albu-Schaffer, and G. Hirzinger, "Integration of reactive, torque-based self-collision avoidance into a task hierarchy," *IEEE TRO*, vol. 28, no. 6, pp. 1278–1293, 2012.

[20] F. Vigoriti, F. Ruggiero, V. Lippiello, and L. Villani, "Control of redundant robot arms with null-space compliance and singularity-free orientation representation," *Robotics and Autonomous Systems*, vol. 100, pp. 186–193, 2018.

[21] D. Guo and Y. Zhang, "Acceleration-level inequality-based man scheme for obstacle avoidance of redundant robot manipulators," *IEEE TIE*, vol. 61, pp. 6903–6914, 2014.

[22] E. M. Hoffman, A. Laurenzi, L. Muratore, N. G. Tsagarakis, and D. G. Caldwell, "Multi-priority cartesian impedance control based on quadratic programming optimization," in *2018 ICRA*. IEEE.

[23] C. Zeng, C. Yang, Z. Jin, and J. Zhang, "Hierarchical impedance, force, and manipulability control for robot learning of skills," *IEEE/ASME Transactions on Mechatronics*, 2024.

[24] K. Dufour and W. Suleiman, "On maximizing manipulability index while solving a kinematics task," *Journal of Intelligent & Robotic Systems*, vol. 100, no. 1, pp. 3–13, 2020.

[25] J. Haviland and P. Corke, "Neo: A novel expeditious optimisation algorithm for reactive motion control of manipulators," *IEEE RA-L*, vol. 6, no. 2, pp. 1043–1050, 2021.